INORGANIC CHEMISTRY FRONTIERS

RESEARCH ARTICLE

View Article Online
View Journal | View Issue

Cite this: *Inorg. Chem. Front.*, 2023, **10**, 1534

A ratiometric fluorescent probe based on a dual-ligand lanthanide metal–organic framework (MOF) for sensitive detection of aluminium and fluoride ions in river and tap water†

Runnan Wang,[a,c] Hao Zhang,[c] Sibo Wang,[a] Fanxu Meng,[d] Jing Sun,*[b] Dawei Lou[c] and Zhongmin Su*[b]

In this study, a ratiometric fluorescent probe towards Al^{3+} and F^- using a lanthanide metal–organic framework material, Eu-BDC-NH_2/TDA, is employed, which is composed of a metal centre Eu^{3+}, BDC-NH_2 and a TDA dual ligand. This three-dimensional frame structure selectively detects Al^{3+} and F^- with a low limit of detection of 0.14 and 0.46 μM, respectively, accompanied by a naked-eye identification specificity in the range of 0–1000 μM. The detection mechanism of Eu-BDC-NH_2/TDA towards Al^{3+} is due to the collapse of the framework and coordination interaction between Al^{3+} and the ligand, and that towards F^- is due to a hydrogen-bond interaction, as evidenced by powder X-ray diffraction, Fourier-transform infrared spectroscopy, X-ray photoelectron spectroscopy and N_2 adsorption–desorption analysis. Furthermore, practical application of Eu-BDC-NH_2/TDA is successful for the detection of Al^{3+} and F^- in river and tap water samples.

Received 30th November 2022,
Accepted 16th January 2023

DOI: 10.1039/d2qi02554j

rsc.li/frontiers-inorganic

1. Introduction

Metal ion pollution, which accompanied the development of the modern industry,[1,2] is detrimental to human health and ecological balance. As the third most abundant essential metal element in the Earth's crust, Al^{3+} and its compounds are extensively used in daily human activities, including water treatment, food processing and pharmaceuticals.[3,4] Owing to such widespread use, Al^{3+} exists widely in the environment and surface water. However, excessive concentrations of Al^{3+} in the human body are toxic and can lead to a wide range of diseases, such as neurotoxicity, breast cancer, liver damage, Parkinson's disease, and Alzheimer's disease.[5–8] The World Health Organization (WHO) has set a maximum limit of 200 μg L^{-1} for Al^{3+} concentration levels in drinking water.[9]

Similarly, anions also play an indispensable role in chemical and biological applications.[10] For example, F^- is important for human and environmental health.[11] In appropriate concentrations it can be used to treat osteoporosis.[12] However, excessive levels of F^- in the human body can lead to a range of negative health effects such as fluorosis, urolithiasis, neurodegenerative diseases, and even death.[13–15] Owing to its toxicity, the WHO advises restricted levels of F^- in drinking water up to 1.50 mg L^{-1}.[16]

Currently, the detection of Al^{3+} and F^- is mostly accomplished through methods such as high-performance liquid chromatography (HPLC), inductively coupled plasma optical emission spectrometry, inductively coupled mass atomic emission spectrometry, atomic absorption spectroscopy, atomic fluorescence spectroscopy (AFS), ion chromatography, Raman spectroscopy, *etc.*[17–19] The limitations of these methods include expensive instrumentation, long hours for analysis, complex sample preparation, and lack of selectivity,[20,21] making them inconvenient for widespread use. Thus, it is vital to explore an accurate and efficient method for detecting them in environmental systems, particularly in drinking water.

[a]*School of Materials Science and Engineering, Changchun University of Science and Technology, Changchun, 130022, People's Republic of China*
[b]*School of Chemistry and Environmental Engineering, Changchun University of Science and Technology, Jilin Provincial Science and Technology Innovation Center of Optical Materials and Chemistry, Jilin Provincial International Joint Research Center of Photo functional Materials and Chemistry, Changchun, 130022, People's Republic of China. E-mail: sj-cust@126.com, zmsu@nenu.edu.cn*
[c]*Department of Analytical Chemistry, Jilin Institute of chemical Technology, Key Laboratory of Fine Chemicals of Jilin Province, Jilin, 132022, PR China*
[d]*Center of Characterization and Analysis, Jilin Institute of Chemical Technology, Jilin, 132022, PR China*

†Electronic supplementary information (ESI) available. CCDC 2219553. For ESI and crystallographic data in CIF or other electronic format see DOI: https://doi.org/10.1039/d2qi02554j

Compared with other analytical methodologies, fluorescent chemosensors have been rapidly developed, owing to their high sensitivity and selectivity, short response time, operational simplicity, low cost, and real-time monitoring ability.[22–24]

Among the various fluorescent materials, lanthanide-based metal–organic frameworks (Ln-MOFs) are considered a promising sensing material owing to their excellent fluorescence performance, which is derived from f–f transitions through an "antenna effect". High colour purity, light emission in the visible range, large Stokes shift, ultrahigh porosity, and tunable structures increase their recognition abilities for analytes.[25–27] For the MOF assay of analytes, the emission signal from fluorescent probes is sufficient for the quantitative analysis of the target analytes; however, it is still easily interfered with by external factors during fluorescence intensity measurements.[28] A dual-emission strategy to construct ratiometric fluorescence sensors can solve the aforementioned problems. Double emission peaks create a self-calibration mechanism that helps to reduce environmental interferences and improve the low detection limit.[29,30] In addition, dual-emission sensors can also make differentiated colours visible to the naked eye.[31] A dual-ligand strategy is an effective approach to achieve dual-emission and specific recognition of a Ln-MOF as a ratiometric fluorescence sensor for targeted analysis. In the dual-ligand Ln-MOF, one ligand sensitizes the Ln^{3+} ion, whereas the other maintains its own emission and performs its own distinct emission. This configuration allows for selective ratiometric sensing and visible detection of the target.[32] Besides, the dual-ligand strategy can simplify the MOF synthesis process to an extent. However, it often requires complex steps, harsh conditions, and expensive raw materials to synthesise a single-ligand framework with multiple different ligand sites and specific configurations. In contrast, a dual/multi-ligand strategy can introduce two/several different types of simple organic ligands to meet the various coordination requirements of metal ions and obtain MOFs with novel structures and excellent properties.[33] However, the sensing ability of dual-ligand ratiometric Ln-MOFs of Al^{3+} and F^- has been rarely studied.

Taking advantage of the excellent optical properties of ratiometric Ln-MOFs, herein, a new dual-emission Eu-MOF [Eu(TDA)(BDC-NH_2)$_{0.5}$(DMA)] (referred to as Eu-BDC-NH_2/TDA) has been synthesised, using 2-aminoterephthalic acid (BDC-NH_2) and 2,5-thiophenedicarboxylic acid (TDA) as the dual ligands, and then structurally characterised. The MOF exhibits good stability in ethanol, high sensitivity and selectivity, good anti-interference ability, and a short response time toward Al^{3+} and F^- upon tuning the emission ratio between the ligand-based and Ln^{3+} metal-based luminescence. Eu(TDA)(BDC-NH_2)$_{0.5}$(DMA) has the ability to detect Al^{3+} and F^- at very low concentrations, with limits of detection as low as 0.14 and 0.46 μM, respectively. This makes it an extremely sensitive fluorescent probe for Al^{3+} and F^- detection. Moreover, to the best of our knowledge, this is the first example of a dual-ligand ratiometric fluorescence Eu-MOF sensor for Al^{3+} and F^- simultaneously.

2. Experimental section

2.1. Synthesis of Eu-BDC-NH_2/TDA

A mixture of $Eu(NO)_3{\cdot}6H_2O$ (0.8921 g, 0.2 mmol), BDC-NH_2 (0.0242 g, 0.14 mmol), TDA (0.0508 g, 0.28 mmol), 2 ml of DMA, and 8 mL of H_2O was stirred for 60 min and then transferred into a 25 mL Teflon-lined stainless steel vessel. After maintaining the mixture at 110 °C for 72 h, the reaction system was slowly cooled to room temperature at a rate of 5 °C h^{-1}. The resulting brown transparent block-like crystals were collected after being washed with DMA and deionised water several times to rid them of excess metals and ligands. The yield of the Eu-BDC-NH_2/TDA crystal was 87%

2.2. Sensing experiment

An Eu-BDC-NH_2/TDA suspension was prepared by dissolving the powder in ethanol at a concentration of 0.2 mg mL^{-1}. Then, 2700 μL of the Eu-BDC-NH_2/TDA suspension and 300 μL of different concentrations of Al^{3+} or F^- solvents were added to 4 mL centrifuge tubes and transferred to quartz cuvettes after 3 min of uniform stirring. The suspensions were immediately monitored for photoluminescence. Emissions between 380 and 660 nm were observed with 1 nm increments under excitation at 361 nm. Finally, the fluorescence intensities of the strong emission peaks at 430 and 621 nm were recorded. A standard calibration curve was created by plotting the fluorescence intensity ratios of I_{430}/I_{621} at Al^{3+}/F^- concentrations in the range of 0–5000 μM, which enables the quantitative measurement of Al^{3+} or F^- in the samples.

In addition, selectivity tests of Eu-BDC-NH_2/TDA were carried out in the presence of the same dosage of interferential metal ion solutions ($M(NO_3)_x$, 0.01 M, M^{x+} = Ca^{2+}, Cu^{2+}, Co^{2+}, Zn^{2+}, Fe^{3+}, Fe^{2+}, Ni^{2+}, Cr^{3+}, K^+, Na^+, NH_4^+, Pb^{2+}, Hg^{2+} Ag^+) and halogen anion solutions (K_xM, 0.01 M, M^{x-} = Cl^-, Br^-, I^-). Furthermore, a 300 μL 0.01 M $M(NO_3)_x$/K_xM solution or H_2O was added to replace Al^{3+} and F^-. Alongside the assay, an anti-interference sensing experiment was conducted by introducing various interfering substances while maintaining the same dosage of Al^{3+} or F^-.

The sensitivity towards Al^{3+} and F^- in the actual water samples was tested using river or tap water replacing deionised water. The river water used was taken from the Jilin section of the Songhua River and filtered, and the tap water was taken from the Key Laboratory of Fine Chemicals of Jilin Province.

3. Results and discussion

3.1. Characterization of the structure

A Cambridge Crystallographic Data Centre (CCDC) number 2219553† was assigned to Eu-BDC-NH_2/TDA by the Cambridge Crystal Database and the details are provided in the ESI (Tables S1–S3†). X-ray single crystal diffraction analysis shows that Eu-BDC-NH_2/TDA crystallised in the triclinic crystal system and the $P\bar{1}(2)$ space group; the asymmetric unit of Eu-BDC-NH_2/TDA is composed of one Eu^{3+} ion, one TDA ligand,

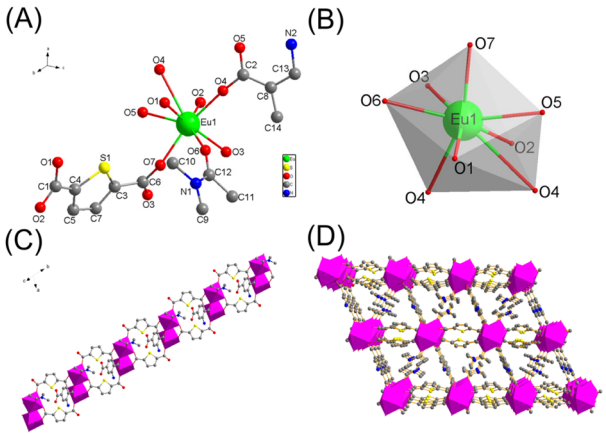

Fig. 1 Crystal structure of Eu-BDC-NH_2/TDA. (A) The asymmetrical unit of Eu-BDC-NH_2/TDA. (B) The coordination environment of the Eu(III) ion. (C) 1D chain formed by the clusters. (D) The 3D frameworks of Eu-BDC-NH_2/TDA.

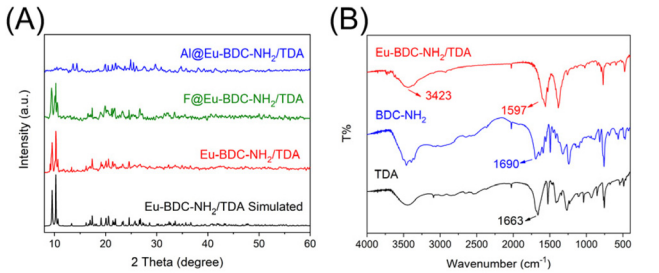

Fig. 2 (A) PXRD patterns of Eu-BDC-NH_2/TDA, Al@Eu-BDC-NH_2/TDA and F@Eu-BDC-NH_2/TDA. (B) FT-IR spectra of TDA, BDC-NH_2 and Eu-BDC-NH_2/TDA.

one half of the BDC-NH_2 ligand and one coordinated DMA molecule (Fig. 1A). There was one crystallographically independent Eu^{3+} ion coordinated by four carboxyl oxygen atoms (O1, O2, O3, and O7) from four TDA ligands, three oxygen atoms (O4, O4, and O5) from 1.5 BDC-NH_2 ligands, and one oxygen atom (O6) from a coordinated DMA molecule, forming a distorted square antiprism coordination geometry (Fig. 1B). The bond lengths of Eu–O that link to TDA range from 2.286(9) to 2.381(5) Å, those of Eu–O that link to BDC-NH_2 range from 2.389(7) to 2.878(6) Å, and those of Eu–O that link to a DMA molecule are 2.372(5) Å. Two Eu^{3+} ion centres are bridged by two carboxylate groups of two TDA ligands and one carboxylate group of BDC-NH_2 to generate a secondary building unit (SBU), and the Eu···Eu distance is 4.047(4) Å. Each Eu2 metallic cluster is connected by the carboxylate groups to form a one-dimensional (1D) chain structure along the *b*-axis (Fig. 1C). These 1D chains are then linked by TDA ligands, together forming a two-dimensional (2D) network along the *ab* plane. The 2D network is further interlinked by BDC-NH_2 ligands to construct a 3D framework (Fig. 1D).

Then, the phase purity of Eu-BDC-NH_2/TDA was ascertained by powder X-ray diffraction analysis (PXRD). As shown in Fig. 2A, the diffraction peaks of the as-synthesised MOF matched the simulated peaks from the single crystal analysis, displaying excellent phase purity and the crystalline nature of Eu-BDC-NH_2/TDA. In addition, the Fourier-transform infrared (FT-IR) spectra in the characteristic absorption peak of BDC-NH_2, TDA, and the as-synthesised Eu-BDC-NH_2/TDA after dehydration in the range of 4000–400 cm^{-1} are listed in Fig. 2B for comparison. Evidently, Eu-BDC-NH_2/TDA and the ligands all have a strong broad peak at 3423 cm^{-1}, which is attributed to the overlap of the stretching vibration of –OH and the stretching vibration of –NH_2.[34,35] After synthesis of the Eu-BDC-NH_2/TDA MOF, the asymmetric stretching peaks of C=O from the carboxyl group at 1663 cm^{-1} in TDA and 1690 cm^{-1} in BDC-NH_2 were significantly blueshifted to 1597 cm^{-1} in Eu-BDC-NH_2/TDA, likely because of the coordination between the carboxylate groups and the Eu^{3+} ions.[36,37] Furthermore, a broad band of approximately 3000 cm^{-1} disappeared from Eu-BDC-NH_2/TDA, demonstrating that the carboxyl group of TDA and BDC-NH_2 were deprotonated to form Eu-BDC-NH_2/TDA successfully.[38]

3.2. Stability of Eu-BDC-NH_2/TDA

Probe materials must possess stability to satisfy practical applications. Ethanol immersion experiments were carried out for seven days. As shown in Fig. S1A,† the fluorescence intensity of the Eu-BDC-NH_2/TDA suspension (0.2 mg mL^{-1}) exhibited negligible change after seven days, and the rate of characteristic emissions of BDC-NH_2 and Eu^{3+}, at 430 and 617 nm respectively, showed slight changes (Fig. S1B†), proving that the structural framework maintains good fluorescence stability in ethanol solution.

Furthermore, thermal gravimetric analysis (TGA) of the Eu-BDC-NH_2/TDA crystal was performed to evaluate the thermal stability and the corresponding spectra were recorded at room temperature to 800 °C (Fig. S2A†). The TGA curve of Eu-BDC-NH_2/TDA showed that it remained stable until 235 °C, whereafter two weight-loss steps were detected. The rate of the first clear weight-loss step was from 235 °C to 335 °C, which corresponds to the loss of DMA molecules with a weight-loss of 18.01% (calculated: 18.06%). The second weight-loss step started at approximately 430 °C, where the collapse of the MOF skeleton, with the loss of BDC-NH_2 and TDA ligands, was observed. This demonstrated the excellent thermal stability of the Eu-BDC-NH_2/TDA framework.

Overall, the immersion and thermal stability experiments indicate that Eu-BDC-NH_2/TDA maintains good thermal and fluorescence stability in the testing environment, making it a promising material for the practical application of sensors.

3.3. Luminescence emission properties of Eu-BDC-NH_2/TDA

To select the optimal medium to achieve the best detection effect, the fluorescence spectra of Eu-BDC-NH_2/TDA dissolved in different organic solvents were investigated. A fully milled sample of 0.6 mg of Eu-BDC-NH_2/TDA was dispersed in different organic solvents, each 3 mL, including isopropanol (IPA), *N,N*-dimethylformamide (DMF), methanol (MeOH),

ethanol (EtOH), benzene (PhH), acetylacetone (AC), acetonitrile (CH_3CN), ethyl ether (Et_2O), *N,N*-dimethylacetamide (DMA), ethylene glycol (EG) and H_2O. The fluorescence spectra are shown in Fig. S2B.† Notably, H_2O displays a remarkably strong emission peak at 430 nm and shows blue fluorescence under UV light, which is disadvantageous for the establishment of ratiometric fluorescent sensors. On the other hand, IPA, DMF, MeOH and EtOH presented stronger emission peaks at 621 nm and a smaller ratio of I_{430}/I_{621} compared to the other organic molecules. In light of these test results, fluorescence detection was performed in an ethanol solvent. Furthermore, response time is also a key aspect of a luminescent probe. As Fig. S3 and S4† show, when Al^{3+} and F^- are added into the Eu-BDC-NH_2/TDA solution, the emission spectrum can reach a transient steady state and the ratio of I_{430}/I_{621} reached a maximum at about 3 min, presenting a quick response time.

The fluorescence spectra of isolated BDC-NH_2, TDA, Eu-BDC-NH_2/TDA and Eu-BDC-NH_2/TDA in a solid state were recorded at room temperature (Fig. 3A). It is observed that BDC-NH_2 possesses a green-yellow fluorescence emission at 566 nm (λ_{ex} = 361 nm), which is attributed to the n–π* or π–π* transitions of BDC-NH_2.[39] Upon the formation of Eu-BDC-NH_2/TDA, the green-yellow fluorescence of BDC-NH_2 decreases, indicating that there exists an energy transfer from BDC-NH_2 to the Eu-MOF.[40] Eu-BDC-NH_2/TDA and Eu-TDA showed the characteristic emission peaks of Eu^{3+} at 594, 621, 655, and 705 nm corresponding to the $^5D_0 \rightarrow {}^7F_J$ (J = 1, 2, 3, 4) transitions,[41] respectively. However, TDA is non-fluorescence, which indicates that TDA can sensitize the fluorescent property of Eu^{3+} ions efficiently. Additionally, this was verified by Reinhold's empirical rule; if the energy gap ΔE ($1\pi\pi^*$–$3\pi\pi^*$) of the ligand is >5000 cm^{-1}, there is an effective intersystem crossing process.[42,43] The singlet-state ($1\pi\pi^*$) level is 39 841 cm^{-1} for H_2TDA[27] and 21 786 cm^{-1} for BDC-NH_2.[44] The triplet-state energy ($3\pi\pi^*$) levels of H_2TDA and BDC-NH_2 are 29 069 cm^{-1} and 17 214 cm^{-1}. The ΔE values of H_2TDA and BDC-NH_2 between S1 and T1 are 18 055 cm^{-1} and 11 855 cm^{-1}, respectively. These two ligands absorb light leading to an effective intersystem crossing process. However, to avoid the dominance of the energy back-transfer process and achieve effective sensitization, ideally, the triplet-state energy needs to be at least 3000 cm^{-1} above the excited state of Ln^{3+}.[45] As a result, the energy difference between the lowest triplet state of H_2TDA and the energy level of Eu^{3+} ions ($^5D_0$) is 4636 cm^{-1} and that of BDC-NH_2 is 62 cm^{-1}. Therefore, BDC-NH_2 is not efficient for sensitizing the fluorescence of Eu^{3+}, whereas H_2TDA is suitable owing to an "antenna effect". The simplified Jablonski diagram of the energy transformation in Eu-BDC-NH_2/TDA is shown in Fig. 3B.

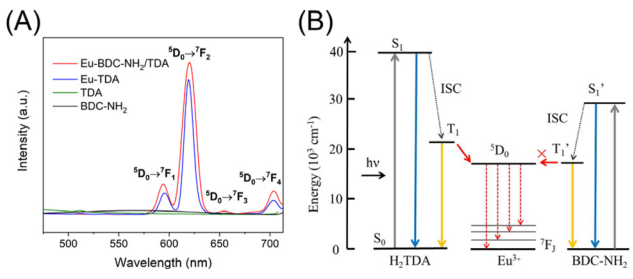

Fig. 3 (A) Solid-state fluorescence spectra of the BDC-NH_2 ligand, TDA ligand, Eu-TDA and Eu-BDC-NH_2/TDA. (B) Simplified Jablonski diagram of the energy transformation in Eu-BDC-NH_2/TDA.

3.4. Ratiometric fluorescent detection of Eu-BDC-NH_2/TDA towards Al^{3+} and F^-

The detection sensitivity of Eu-BDC-NH_2/TDA as a sensor for Al^{3+}/F^- is an important criterion. To evaluate the relationship between the changes in the luminescence intensities of Eu-BDC-NH_2/TDA and concentrations of Al^{3+}/F^-, corresponding experiments were performed by gradually adding Al^{3+} or F^- with different concentration gradients (0–5000 μM) into well-dispersed ethanol suspensions of Eu-BDC-NH_2/TDA, and the intensities of 430 and 621 nm transition were monitored. The fluorescence spectra at different concentrations of Al^{3+} are shown in Fig. 4A, and the luminescence intensity variations at 430 and 621 nm are listed in Fig. 4B. Those of F^- are listed in Fig. 5A and B. As the concentrations of Al^{3+} and F^- increased, the fluorescence intensity at 621 nm decreased gradually, while the fluorescence at 430 nm recovered and exhibited blue-shift simultaneously, resulting in the rise of the I_{430}/I_{621} value. As shown in Fig. 4C and 5C, the I_{430}/I_{621} value increases linearly as the Al^{3+} or F^- concentration increases and a good linear relationship (Y = 2.31919 + 0.19573X (R^2 = 0.99021), Y = −0.35952 + 0.1025X (R^2 = 0.99751) is obtained between 0 and 1000 μM. Furthermore, the limits of detection (LODs) ($3\sigma/k$) of Al^{3+} and F^- were calculated to be 0.14 and 0.46 μM, far lower

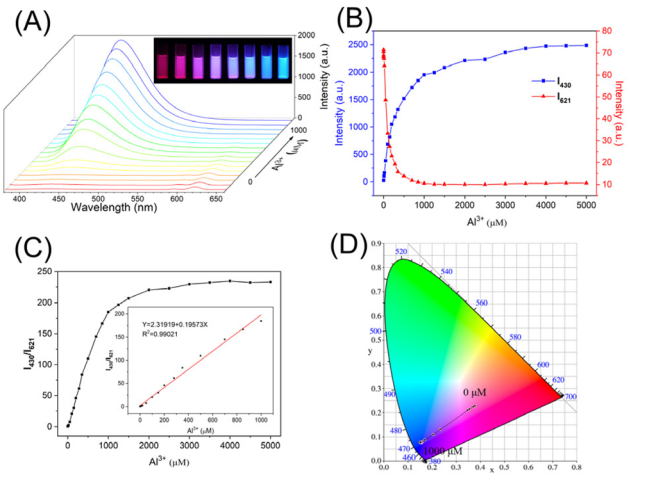

Fig. 4 (A) Fluorescence emission spectra of Eu-BDC-NH_2/TDA in the presence of different concentrations of Al^{3+}. (B) Relationship between the luminescence intensities of 433 and 621 nm and the Al^{3+} concentration in Eu-BDC-NH_2/TDA. (C) Change of the I_{430}/I_{621} upon an increase in the Al^{3+} concentration, inset: linear relationship between the I_{430}/I_{621} and concentration of Al^{3+} in the range of 0–1000 μM. (D) CIE chromaticity diagram of Eu-BDC-NH_2/TDA in the presence of different concentrations of Al^{3+} from 0 to 1000 μM.

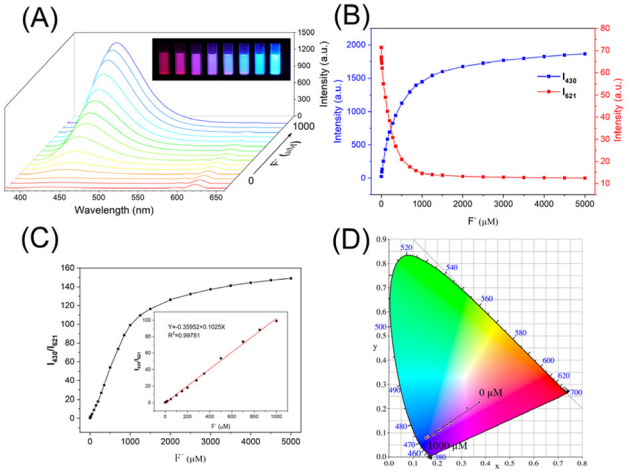

Fig. 5 (A) Fluorescence emission spectra of Eu-BDC-NH_2/TDA in the presence of different concentrations of F^-. (B) Relationship between the luminescence intensities of 433 and 621 nm and the F^- concentration in Eu-BDC-NH_2/TDA. (C) Change of the I_{430}/I_{621} upon the increase of the F^- concentration, inset: linear relationship between the I_{430}/I_{621} and the concentration of F^- in the range of 0–1000 μM. (D) CIE chromaticity diagram of Eu-BDC-NH_2/TDA in the presence of different concentrations of F^- from 0 to 1000 μM.

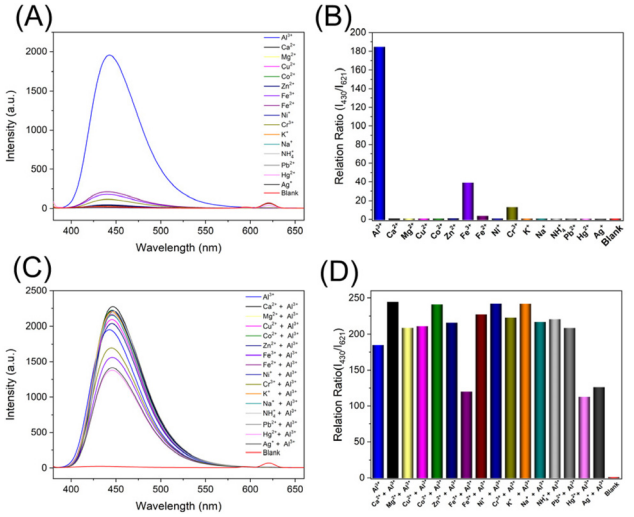

Fig. 6 (A) The fluorescence and (B) the intensity ratio of I_{430}/I_{621} of Eu-BDC-NH_2/TDA responding to different metal cations. (C) The fluorescence and (D) the intensity ratio of I_{430}/I_{621} of Eu-BDC-NH_2/TDA responding to Al^{3+} with other different metal cations as the interference.

than that of the WHO standard for drinking water. This implies that Eu-BDC-NH_2/TDA can be considered an effective material for monitoring Al^{3+} and F^- concentrations in drinking water.

Additionally, the response of BDC-NH_2 to Al^{3+} and F^- with different concentrations was tested. The results showed that the BDC-NH_2 emissions at 430 nm intensified gradually as the Al^{3+} and F^- concentrations increased, displaying a strong linear relationship (Fig. S5 and S6†). Compared with Eu-BDC-NH_2/TDA, only a single blue emission of BDC-NH_2 was observed in both CIE chromaticity coordinates and observation with the naked eye (Fig. S7A and S7B†). For this ratiometric probe, the emission colour changed from red to blue obviously as the Al^{3+} or F^- concentration increased under illumination with UV light (254 nm) when observed through the naked eye (Fig. 4A and 5A inset). As illustrated in Fig. 4D and 5D, the CIE chromaticity coordinates further confirmed that the fluorescent colour of Eu-BDC-NH_2/TDA exhibits an obvious colour transition from red to blue induced by Al^{3+}/F^- ions, thereby providing a convenient visual analysis towards Al^{3+} and F^- ions.

High selectivity and anti-interference ability can be regarded as indispensable features in evaluating the performance of fluorescent probes. Consequently, we investigated the emission spectra of Eu-BDC-NH_2/TDA in ethanol solution with the addition of different metal cations and halogenide anions, including Ca^{2+}, Cu^{2+}, Co^{2+}, Zn^{2+}, Fe^{3+}, Fe^{2+}, Ni^{2+}, Cr^{3+}, K^+, Na^+, NH_4^+, Pb^{2+}, Hg^{2+}, Ag^+, Cl^-, Br^-, and I^-. All the fluorescence measurements were performed under the same conditions. As shown in Fig. 6A, B, S8A, and S8C,† the experimental results demonstrate that all the selected ions exhibit negligible changes in the fluorescence spectrum and ratio of I_{430}/I_{621} excepted Al^{3+} and F^-.

Concurrently, anti-interferential experiments were carried out in the presence of the same concentration of metal cations as interferences. As shown in Fig. 6C, D, S8B, and S8C,† the fluorescence that occurred in the presence of Al^{3+}/F^- is unaffected by the coexisting interferences, suggesting that Eu-BDC-NH_2/TDA has excellent specificity and anti-interference abilities for Al^{3+} and F^- detection in complex practical samples.

3.5. A possible response mechanism of Eu-BDC-NH_2/TDA towards Al^{3+} and F^- ions

To further investigate the fluorescence variation mechanism, PXRD, FT-IR and X-ray photoelectron spectroscopy (XPS) of Eu-BDC-NH_2/TDA were carried out before and after testing Al^{3+} (Al@Eu-BDC-NH_2/TDA) and F^- (F@Eu-BDC-NH_2/TDA). First, comparing the PXRD pattern of Al@Eu-BDC-NH_2/TDA to that of Eu-BDC-NH_2/TDA (Fig. 2A), a significant pattern difference was observed. The characteristic peaks of 5–15° disappeared in the original crystal, which implied a possible change attributed to the collapse of the crystal structure.[46] As a result of the collapse, BDC-NH_2 was released, emitting blue fluorescence at 430 nm, which is consistent with the free BDC-NH_2 molecules.[47] Additionally, XPS analyses for Eu-BDC-NH_2/TDA and Al@Eu-BDC-NH_2/TDA were also performed to further assess the mechanisms. As seen in Fig. 7A and B, the characteristic peak of Al was visible at 75.08 eV in the XPS spectra of Al@Eu-BDC-NH_2/TDA, indicating that Al^{3+} ions combined within Eu-BDC-NH_2/TDA. Furthermore, the N_2 adsorption–desorption isotherms of Eu-BDC-NH_2/TDA and Al@Eu-BDC-NH_2/TDA were obtained at 77 K (Fig. S9A†). The isotherm behaviour of both materials displays a classical Type I shape, indicating

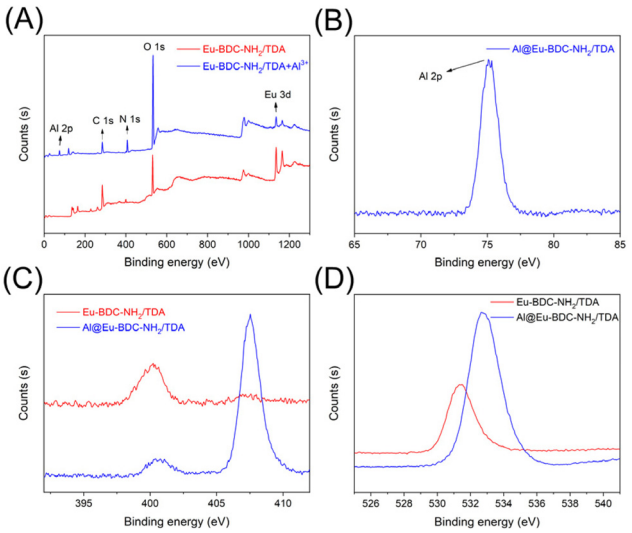

Fig. 7 (A) XPS spectra for Eu-BDC-NH_2/TDA and Al@Eu-BDC-NH_2/TDA. (B) XPS spectra for Al2p in Al@Eu-BDC-NH_2/TDA. (C) XPS spectra for N1s in Eu-BDC-NH_2/TDA and Al@Eu-BDC-NH_2/TDA. (D) XPS spectra for O1s in Eu-BDC-NH_2/TDA and Al@Eu-BDC-NH_2/TDA.

that they are microporous materials. The Brunauer–Emmett–Teller (BET) specific surface areas of Eu-BDC-NH_2/TDA and Al@Eu-BDC-NH_2/TDA are 2056.05 and 1490.47 $m^2\ g^{-1}$, respectively. The pore size distributions of Eu-BDC-NH_2/TDA are mainly situated at 0.63 nm, whereas those of Al@Eu-BDC-NH_2/TDA are at 0.84, 0.86 and 0.88 nm. After the treatment with Al^{3+} ions, the pore structure changed, the specific surface area of the MOF decreased, the pore size distribution widened, and multiple micropores appeared, which infer an MOF frame structure collapse.[48]

In addition to the frame collapse, another possible mechanism is a coordinating interaction according to the FT-IR spectrum of Eu-BDC-NH_2/TDA and Al@Eu-BDC-NH_2/TDA. As shown in Fig. S10,† the FT-IR spectra of Al@Eu-BDC-NH_2/TDA present a new absorption band at 596 cm^{-1}. This is ascribed to the stretching vibration of Al–O,[49] peaking at 1560 cm^{-1}, which belongs to the asymmetric stretching of –COO that decreased significantly, possibly explaining the coordination between Al^{3+} and –COO.[50,51]

Furthermore, XPS spectra can also prove the presence of coordination interaction between the MOF and the analyte. According to the peak positions of N1s and O1s orbitals in Eu-BDC-NH_2/TDA and Al@Eu-BDC-NH_2/TDA, the N1s peak in the N1s XPS spectrum of Eu-BDC-NH_2/TDA only showed one peak at 400.23 eV, whereas the Al@Eu-BDC-NH_2/TDA spectrum showed two peaks at 407.53 and 400.38 eV. The new peak at 407.53 eV can be assigned to N–Al, demonstrating the coordination of Al^{3+} to the N atom from BDC-NH_2.[52] Another N1s peak shifted from 400.23 to 400.38 eV (Fig. 7C), and the O1s peak changed from 531.48 to 532.68 eV (Fig. 7D). This suggests a decrease in electron density around the N and O atoms, indicating that there may exist coordination interactions between Al and N, as well as Al and O from the ligand.[37,53,54] According to these findings, Eu-BDC-NH_2/TDA plays a leading role in the collapse of frame and coordination interaction during Al^{3+} sensing.

The mechanism for detecting F^- differs from that for detecting Al^{3+}. As exhibited in Fig. 2A, the PXRD pattern of F@Eu-BDC-NH_2/TDA is almost identical to that of Eu-BDC-NH_2/TDA, which demonstrates that structural reorganisation or collapse is not a sensing mechanism. Moreover, in the water response experiment for Eu-BDC-NH_2/TDA that was conducted to explain the reaction mechanism between the MOF and F^- (Fig. S11†), the blue fluorescence at 430 nm increased and the red fluorescence at 621 nm decreased as the content of water/ethanol in the MOF solution gradually increased. It is speculated that the BDC-NH_2 in Eu-BDC-NH_2/TDA is protonated by water to form BDC-NH^{3+}[55] and then interacts with F^- to form an N–H···F hydrogen bond structure, so as to shorten the distance between the MOF and F^- and realise an efficient energy transfer.[56] This is also demonstrated by the XPS of Eu-BDC-NH_2/TDA and F@Eu-BDC-NH_2/TDA. The formation of the N–H···F hydrogen bond shortened the distance between N and F, thus affecting the electron cloud density around N, resulting in the shift of the N1s peak from 400.20 to 400.15 eV (Fig. S12B†). Additionally, the O1s peak in the O1s XPS spectrum of Eu-BDC-NH_2/TDA and F@Eu-BDC-NH_2/TDA did not shift, indicating that F^- did not coordinate with O (Fig. S12C†). Fig. S10A† shows the FT-IR spectra of Eu-BDC-NH_2/TDA and F@Eu-BDC-NH_2/TDA and the detailed enlargement is shown in Fig. S10B.† The peaks at 3437.97 cm^{-1} and 1560.61 cm^{-1}, which are attributed to the stretching and bending vibrations of $-NH_2$ in Eu-BDC-NH_2/TDA, are red shifted to 3442.92 cm^{-1} and 1568.83 cm^{-1} in F@Eu-BDC-NH_2/TDA, confirming the presence of the N–H···F hydrogen bond.[35] Finally, the channels of the MOF structure were studied. As observed in Fig. S13,† the four neighbouring Eu^{3+} ions along the *a* direction form a rhombic shape window (size: 4.9301 × 13.8147 $Å^2$). The MOF channel is partially occupied by free DMA molecules, resulting in the pore window being separated and significantly reduced. The aperture is an irregular shape and the insertable virtual spherical atom has a diameter of 3.74 Å. The diameters of F^-, Cl^-, Br^-, and I^- are about 2.72 Å, 3.62 Å, 3.90 Å, and 4.32 Å,[57] respectively. It is likely that the smaller diameter of F^- allows it to enter the pore of Eu-BDC-NH_2/TDA and form hydrogen bonds with the amino groups in the pores. In contrast, the diameters of Cl^-, Br^-, and I^- are greater than or close to the size of the channel, which makes them difficult or unable to diffuse into the channel of the MOF. This may explain why Eu-BDC-NH_2/TDA has unique F^- sensing capabilities.

3.6. Sensing Al^{3+} and F^- ions in real water samples

To estimate the practical application of Eu-BDC-NH_2/TDA, we analysed different concentrations of Al^{3+} or F^- in tap and river water using the proposed ratiometric method. The recovery tests were carried out six times and the experimental results are shown in Table 1; the recoveries were in the range of 97.85–105.05%, and the relative standard deviation (RSD) is

Table 1 Determination of Al^{3+} and F^- in real water samples using the standard addition method

Samples	Added (μM)	Found (μM)	Recovery %	RSD % $N = 6$
Tap water + Al^{3+}	100	98.29	98.29	2.6
	200	207.76	103.88	2.4
	500	512.76	102.55	1.2
Songhua river + Al^{3+}	100	101.54	101.54	3.2
	200	208.10	104.05	2.5
	500	525.28	105.05	2.4
Tap water + F^-	100	97.85	97.85	3.3
	200	209.42	104.71	2.7
	500	509.7	101.94	1.8
Songhua river + F^-	100	98.36	98.36	3.1
	200	206.82	103.41	2.3
	500	518.15	103.63	1.5

less than 3.3%, which displays acceptable precision and satisfactory reproducibility, indicating that Eu-BDC-NH_2/TDA is a feasible and reliable probe for measuring Al^{3+} and F^- for practical application.

4. Conclusions

In summary, a dual-emission MOF fluorescent probe, Eu-BDC-NH_2/TDA, was rationally designed and successfully synthesised using a simple solvothermal method. This ratiometric probe showed exceptional sensitivity, high selectivity, low LOD, excellent anti-interference characteristics as well as direct visual observation toward Al^{3+} and F^- in an ethanol medium. The study on the sensor mechanism implied that the fluorescence changes of Eu-BDC-NH_2/TDA towards Al^{3+} could be due to a framework collapse and coordination interaction. The mechanism of Eu-BDC-NH_2/TDA towards F^- could be due to a hydrogen-bond interaction. Moreover, this probe also showed satisfactory repeatability and recovery rates when applied to river and tap water samples. Given these merits, we believe that the Eu-BDC-NH_2/TDA fluorescent probe exhibits enormous potential for monitoring Al^{3+} and F^- with practical applications.

Author contributions

The authors contributed equally to this work.

Conflicts of interest

There are no conflicts to declare.

Acknowledgements

This work was financially supported by the Natural Science Foundation of Jilin Province (20220101082JC).

References

1 W. Li, C. Jiang, S. Lu, F. Wang, Z. Zhang, T. Wei, Y. Chen, J. Qiang, Z. Yu and X. Chen, A hydrogel microsphere-based sensor for dual and highly selective detection of Al^{3+} and Hg^{2+}, *Sens. Actuators, B*, 2020, **321**, 128490.
2 L. Zhang, B. Zhao, G. Xu and Y. Guan, Characterizing fluvial heavy metal pollutions under different rainfall conditions: Implication for aquatic environment protection, *Sci. Total Environ.*, 2018, **635**, 1495–1506.
3 N. Xiao, L. Xie, X. Zhi and C. Fang, A naphthol-based highly selective fluorescence turn-on and reversible sensor for Al(III) ion, *Inorg. Chem. Commun.*, 2018, **89**, 13–17.
4 R. Li, Z. Wei, L. Wang, Y. Zhang and J. Ru, A new salamo-based fluorescence probe to visually detect aluminum(III) ion and bio-imaging in zebrafish, *Microchem. J.*, 2021, **162**, 105720.
5 S. Goswami, S. Paul and A. Manna, Selective "naked eye" detection of Al(iii) and PPi in aqueous media on a rhodamine-isatin hybrid moiety, *RSC Adv.*, 2013, **3**, 10639–10643.
6 S. Zeng, S. Li, X. Sun, M. Li, Z. Xing and J. Li, A benzothiazole-based chemosensor for significant fluorescent turn-on and ratiometric detection of Al^{3+} and its application in cell imaging, *Inorg. Chim. Acta*, 2019, **486**, 654–662.
7 G. D. Fasman, Aluminum and Alzheimer's disease: model studies, *Coord. Chem. Rev.*, 1996, **149**, 125–165.
8 D. Aydin, A novel turn on fluorescent probe for the determination of Al^{3+} and Zn^{2+} ions and its cells applications, *Talanta*, 2020, **210**, 120615.
9 V. K. Gupta, N. Mergu, L. K. Kumawat and A. K. Singh, A reversible fluorescence "off-on-off" sensor for sequential detection of aluminum and acetate/fluoride ions, *Talanta*, 2015, **144**, 80–89.
10 G. Sivaraman and D. Chellappa, Rhodamine based sensor for naked-eye detection and live cell imaging of fluoride ions, *J. Mater. Chem. B*, 2013, **1**, 5768–5772.
11 S. Xu, K. Chen and H. Tian, A colorimetric and fluorescent chemodosimeter: fluoride ion sensing by an axial-substituted subphthalocyanine, *J. Mater. Chem.*, 2005, **15**, 2676–2680.
12 R. Hu, J. Feng, D. Hu, S. Wang, S. Li, Y. Li and G. Yang, A Rapid Aqueous Fluoride Ion Sensor with Dual Output Modes, *Angew. Chem., Int. Ed.*, 2010, **49**, 4915–4918.
13 T. Hudnall, C. Chiu and F. Gabbaï, Fluoride Ion Recognition by Chelating and Cationic Boranes, *Acc. Chem. Res.*, 2009, **42**, 388–397.
14 B. Aradhyula, R. Ranga, K. Dhanunjayarao and K. Venkatasubbaiah, Synthesis and characterization of poly(tetraphenylimidazole)s and their application in the detection of fluoride ions, *RSC Adv.*, 2020, **10**, 13149–13154.
15 A. L. Choi, G. Sun, Y. Zhang and P. Grandjean, Developmental Fluoride Neurotoxicity: A Systematic Review and Meta-Analysis, *Environ. Health Perspect.*, 2012, **120**, 1362–1368.

16 Y. Qin, A. Faheem and Y. Hu, A spore-based portable kit for on-site detection of fluoride ions, *J. Hazard. Mater.*, 2021, **419**, 126467.
17 M. Ahmad and R. Narayanaswamy, Optical fibre Al(III) sensor based on solid surface fluorescence measurement, *Sens. Actuators, B*, 2002, **81**, 259–266.
18 Y. Zhou, J. F. Zhang and J. Yoon, Fluorescence and Colorimetric Chemosensors for Fluoride-Ion Detection, *Chem. Rev.*, 2014, **114**, 5511–5571.
19 G. Aragay, J. Pons and A. Merkoçi, Recent Trends in Macro-, Micro-, and Nanomaterial-Based Tools and Strategies for Heavy-Metal Detection, *Chem. Rev.*, 2011, **111**, 3433–3458.
20 M. Sun and Q. Wu, Determination of ultra-trace aluminum in human albumin by cloud point extraction and graphite furnace atomic absorption spectrometry, *J. Hazard. Mater.*, 2010, **176**, 901–905.
21 T. Xuan, Y. Gao, Y. Cai, X. Guo, Y. Wen and H. Yang, Fabrication and characterization of the stable Ag-Au-metal-organic-frameworks: An application for sensitive detection of thiabendazole, *Sens. Actuators, B*, 2019, **293**, 289–295.
22 T. Sun, R. Fan, R. Xiao, T. Xing, M. Qin, Y. Liu, S. Hao, W. Chen and Y. Yang, Anionic Ln-MOF with tunable emission for heavy metal ion capture and l-cysteine sensing in serum, *J. Mater. Chem. A*, 2020, **8**, 5587–5594.
23 H. Yin, X. Wang and X. Yin, Rotation Restricted Emission and Antenna Effect in Single Metal-Organic Frameworks, *J. Am. Chem. Soc.*, 2019, **141**, 15166–15173.
24 T. Sun, P. Wang, R. Fan, W. Chen, S. Hao and Y. Yang, Functional microscale single-phase white emission lanthanide MOF for tunable fluorescent sensing and water quality monitoring, *J. Mater. Chem. C*, 2019, **7**, 3598–3606.
25 T. Luo, C. Liu, S. V. Eliseeva, P. F. Muldoon, S. Petoud and N. L. Rosi, Rare Earth pcu Metal-Organic Framework Platform Based on $RE_4(\mu_3\text{-}OH)_4(COO)_6^{2+}$ Clusters: Rational Design, Directed Synthesis, and Deliberate Tuning of Excitation Wavelengths, *J. Am. Chem. Soc.*, 2017, **139**, 9333–9340.
26 X. Li, S. Lu, D. Tu, W. Zheng and X. Chen, Luminescent lanthanide metal-organic framework nanoprobes: from fundamentals to bioapplications, *Nanoscale*, 2020, **12**, 15021–15035.
27 S. Wu, Y. Lin, J. Liu, W. Shi, G. Yang and P. Cheng, Rapid Detection of the Biomarkers for Carcinoid Tumors by a Water Stable Luminescent Lanthanide Metal-Organic Framework Sensor, *Adv. Funct. Mater.*, 2018, **28**, 1707169.
28 K. Komatsu, Y. Urano, H. Kojima and T. Nagano, Development of an Iminocoumarin-Based Zinc Sensor Suitable for Ratiometric Fluorescence Imaging of Neuronal Zinc, *J. Am. Chem. Soc.*, 2007, **129**, 13447–13454.
29 W. Li, X. Zhang, X. Hu, Y. Shi, Z. Li, X. Huang, W. Zhang, D. Zhang, X. Zou and J. Shi, A smartphone-integrated ratiometric fluorescence sensor for visual detection of cadmium ions, *J. Hazard. Mater.*, 2021, **408**, 124872.
30 S. Wu, H. Min, W. Shi and P. Cheng, Multicenter Metal-Organic Framework-Based Ratiometric Fluorescent Sensors, *Adv. Mater.*, 2020, **32**, 1805871.
31 L. Chen, D. Liu, J. Peng, Q. Du and H. He, Ratiometric fluorescence sensing of metal-organic frameworks: Tactics and perspectives, *Coord. Chem. Rev.*, 2020, **404**, 213113.
32 Y. Xia, Y. Sun, Y. Cheng, Y. Xia and X. Yin, Rational design of dual-ligand Eu-MOF for ratiometric fluorescence sensing Cu^{2+} ions in human serum to diagnose Wilson's disease, *Anal. Chim. Acta*, 2022, **1204**, 339731.
33 H. Furukawa, K. E. Cordova, M. O'Keeffe and O. M. Yaghi, The Chemistry and Applications of Metal-Organic Frameworks, *Science*, 2013, **341**, 1230444.
34 K. Yi, H. Li, X. Zhang and L. Zhang, Designed Tb(III)-Functionalized MOF-808 as Visible Fluorescent Probes for Monitoring Bilirubin and Identifying Fingerprints, *Inorg. Chem.*, 2021, **60**, 3172–3180.
35 J. Ma, Y. Shen, C. Shen, Y. Wen and W. Liu, Al-doping chitosan-Fe(III) hydrogel for the removal of fluoride from aqueous solutions, *Chem. Eng. J.*, 2014, **248**, 98–106.
36 J. Xiao, M. Liu, F. Tian and Z. Liu, Stable Europium-based Metal-Organic Frameworks for Naked-eye Ultrasensitive Detecting Fluoroquinolones Antibiotics, *Inorg. Chem.*, 2021, **60**, 5282–5289.
37 X. Zhang, Q. Ma, X. Liu, H. Niu, L. Luo, R. Li and X. Feng, A turn-off Eu-MOF@Fe^{2+} sensor for the selective and sensitive fluorescence detection of bromate in wheat flour, *Food Chem.*, 2022, **382**, 132379.
38 Y. Sun, Y. Cheng and X. Yin, Dual-Ligand Lanthanide Metal-Organic Framework for Sensitive Ratiometric Fluorescence Detection of Hypochlorous Acid, *Anal. Chem.*, 2021, **93**, 3559–3566.
39 S. Zhao, G. Wang, D. Poelman and P. V. D. Voort, Luminescent Lanthanide MOFs: A Unique Platform for Chemical Sensing, *Materials*, 2018, **11**, 572.
40 M. Yu, Y. Xie, X. Wang, Y. Li and G. Li, Highly Water-Stable Dye@Ln-MOFs for Sensitive and Selective Detection toward Antibiotics in Water, *ACS Appl. Mater. Interfaces*, 2019, **11**, 21201–21210.
41 N. Zhang, Q. Guan, C. Liu, Y. Sun, B. Li, Y. Xing and F. Bai, A rht-Type Luminescent Zn(II)-MOF Constructed by Triazine Hexacarboxylate Ligand: Tunable Luminescent Performance and White-light Emission Regulation through doping Eu^{3+}/Tb^{3+}, *Appl. Organomet. Chem.*, 2020, **34**, e5506.
42 F. J. Steemers, W. Verboom, D. N. Reinhoudt, E. B. van der Tol and J. W. Verhoeven, New Sensitizer-Modified Calix[4]arenes Enabling Near-UV Excitation of Complexed Luminescent Lanthanide Ions, *J. Am. Chem. Soc.*, 1995, **117**, 9408–9414.
43 S. Wang, B. Sun, Z. Su, G. Hong, X. Li, Y. Liu, Q. Pan and J. Sun, Lanthanide-MOFs as multifunctional luminescent sensors, *Inorg. Chem. Front.*, 2022, **9**, 3259–3266.
44 X. Wang, Y. Wang, X. Wang, C. Hu, X. Wu, W. Guo, S. Zhen, C. Huang and Y. Li, Dual-ligand two-dimensional Europium-organic gels nanosheets for ratiometric fluo-

rescence detecting anthrax spore biomarker, *Chem. Eng. J.*, 2022, **435**, 134912.
45 H. Yin and X. Yin, Multi-Emission from Single Metal–Organic Frameworks under Single Excitation, *Small*, 2022, **18**, 2106587.
46 S. Dang, E. Ma, Z. Sun and H. Zhang, A layer-structured Eu-MOF as a highly selective fluorescent probe for Fe^{3+} detection through a cation-exchange approach, *J. Mater. Chem.*, 2012, **22**, 16920–16926.
47 B. Wang and B. Yan, A dye@MOF crystalline probe serving as a platform for ratiometric sensing of trichloroacetic acid (TCA), a carcinogen metabolite in human urine, *CrystEngComm*, 2019, **21**, 4637–4643.
48 J. E. Mondloch, O. Karagiaridi, O. K. Farha and J. T. Hupp, Activation of metal–organic framework materials, *CrystEngComm*, 2013, **15**, 9258–9264.
49 K. Yi and L. Zhang, Designed Eu(III)-functionalized nanoscale MOF probe based on fluorescence resonance energy transfer for the reversible sensing of trace Malachite green, *Food Chem.*, 2021, **354**, 129584.
50 X. Zhang, L. Fang, K. Jiang, H. He, Y. Yang, Y. Cui, B. Li and G. Qian, Nanoscale fluorescent metal-organic framework composites as a logic platform for potential diagnosis of asthma, *Biosens. Bioelectron.*, 2019, **130**, 65–72.
51 X. Zhang, Q. Hu, T. Xia, J. Zhang, Y. Yang, Y. Cui, B. Chen and G. Qian, Turn-on and Ratiometric Luminescent Sensing of Hydrogen Sulfide Based on Metal-Organic Frameworks, *ACS Appl. Mater. Interfaces*, 2016, **8**, 32259–32265.
52 X. Wang, Y. Wang, X. Wang, K. Lu, W. Jiang, P.-P. Cui, H. Hao and F. Dai, Two series of Ln-MOFs by solvent induced self-assembly demonstrating the rapid selective sensing of Mg^{2+} and Fe^{3+} cations, *Dalton Trans.*, 2020, **49**, 15473–15480.
53 X. Peng, G. Bao, Y. Zhong, L. Zhang, K. Zeng, J. He, W. Xiao, Y. Xia, Q. Fan and H. Yuan, Highly sensitive and rapid detection of thiabendazole residues in oranges based on a luminescent Tb^{3+}-functionalized MOF, *Food Chem.*, 2021, **343**, 128504.
54 G. Qin, J. Wang, L. Li, F. Yuan, Q. Zha, W. Bai and Y. Ni, Highly water-stable Cd-MOF/Tb^{3+} ultrathin fluorescence nanosheets for ultrasensitive and selective detection of Cefixime, *Talanta*, 2021, **221**, 121421.
55 H. Yin, J. Yang and X. Yin, Ratiometric Fluorescence Sensing and Real-Time Detection of Water in Organic Solvents with One-Pot Synthesis of Ru@MIL-101(Al)–NH2, *Anal. Chem.*, 2017, **89**, 13434–13440.
56 Y. Dong, G. Li, N. Zhou, R. Wang, Y. Chi and G. Chen, Graphene Quantum Dot as a Green and Facile Sensor for Free Chlorine in Drinking Water, *Anal. Chem.*, 2012, **84**, 8378–8382.
57 E. R. Nightingale Jr., Phenomenological Theory of Ion Solvation. Effective Radii of Hydrated Ions, *J. Phys. Chem.*, 1959, **63**, 1381–1387.

